Arabian Journal for Science and Engineering (2025) 50:3417–3434
https://doi.org/10.1007/s13369-024-09489-2

RESEARCH ARTICLE - SPECIAL ISSUE - CHALLENGES AND RECENT ADVANCEMENTS IN NUCLEAR ENERGY SYSTEMS

Experimental and Numerical Study of Taylor Bubble in Counter-Current Turbulent Flow

Iztok Tiselj[1,2] · Jan Kren[1,2] · Blaž Mikuž[1] · Raksmy Nop[3] · Alan Burlot[3] · Grégoire Hamrit[3]

Received: 11 March 2024 / Accepted: 28 July 2024 / Published online: 21 August 2024

Abstract
The stagnant Taylor bubble in vertical isothermal turbulent counter-current flow was analyzed using 2D shadowgraphy experiments and two distinct high-fidelity numerical simulations. One simulation employed the geometrical VOF interface tracking method within the OpenFOAM code, while the other utilized the explicit front tracking method of the TrioCFD code. Interface recognition algorithms were applied to the photographs and compared with the results of 3D simulations performed with LES and pseudo-DNS accuracy in OpenFOAM and TrioCFD, respectively. The measured Taylor bubbles exhibited an asymmetric bullet-train shape and a specific speed, which were compared with the predictions of both numerical approaches. Reproducing the experiment proved challenging for both otherwise well-established methods frequently used in interface tracking simulations of two-phase flows. Grid resolution and subgrid turbulent models, known for their success in single-phase turbulence, were less accurate near the water–air interface. Additional experimental parameters compared with simulations were related to the dynamics of tiny disturbance waves with amplitudes ranging from 10 to 100 μm along the interface of the Taylor bubbles. The speed and spectra of the surface disturbance waves were reproduced numerically with moderate success despite detailed grid refinement in the relevant region of the computational domain.

Keywords Slug flow · Taylor bubble · Shadowgraphy · VOF interface capturing · Front tracking

1 Introduction

Gas–liquid mixture flows exhibit various two-phase flow patterns, with vertical pipes commonly experiencing bubbly, slug, churn, annular, and droplet flow regimes [1]. The specific flow regime depends on factors such as flow velocities, phase volume fractions, fluid properties, pipe size, and orientation. This study is focused on Taylor bubble flow, which falls under the slug flow regime. Taylor bubbles are bullet-shaped bubbles that move at different speeds from the bulk liquid, occupying almost the entire pipe cross section. Slug flows are relevant for chemical, nuclear, petroleum, and other types of processing engineering. They are encountered in a wide range of practical applications, including vaporizers, boilers, filtration and membrane processes [2], as well as extreme events in the petroleum industry [3] or steam generators in nuclear power plants. The most recent review paper discussing vertical gas–liquid slug flows by Holagh & Ahmed from 2024 [4] demonstrates the extensive scope of this research area. This remarkable review is citing 470 references.

✉ Iztok Tiselj
iztok.tiselj@ijs.si

Jan Kren
jan.kren@ijs.si

Blaž Mikuž
blaz.mikuz@ijs.si

Raksmy Nop
raksmy.nop@cea.fr

Alan Burlot
alan.burlot@cea.fr

Grégoire Hamrit
gregoire.hamrit@cea.fr

1 Jožef Stefan Institute, Jamova 39, 1000 Ljubljana, Slovenia

2 Faculty of Mathematics and Physics, University of Ljubljana, Jadranska Ulica 19, 1000 Ljubljana, Slovenia

3 Service de Thermohydraulique Et de Mécanique Des Fluides, Université Paris-Saclay, CEA, 91191 Gif-Sur-Yvette, France

The type of slug flows relevant to the present study occurs in the inertia-dominant regime, where the influence of viscosity and surface tension is minimal [1]. In this regime, the drift velocity of Taylor bubbles U_0 in pipe with diameter D is given by the correlation $U_0 = k\sqrt{gD}$ (g acceleration of gravity). Based on the constant value of $k \approx 0.35$, this correlation predicts a drift velocity of approximately 0.18 m/s for Taylor bubbles in our experiments [5]. This value is close to the average measured liquid velocity, U_L, which is in the downward direction (negative sign) and keeps the bubble fixed in position. Dumitrescu [6] demonstrated that soon after the liquid flow was directed downward, the Taylor bubble became unstable. One of the earliest detailed experiments on counter-current turbulent flow was performed by Martin [7], who studied air–water mixtures in circular pipes with diameters of 2.6, 10.16, and 14.0 cm. Martin found that the bubble velocity in counter-current slug flow could not be adequately explained by existing theories for co-current background flow or stagnant liquid conditions. This discrepancy is due to bubble instability, which increases bubble velocity when the bubble is displaced from the pipe axis. Lu and Prosperetti [8] performed a stability analysis and showed that the breakup of Taylor bubble symmetry occurs at liquid velocities below a critical negative velocity of $U_c = -0.13\sqrt{gD}$. Figueroa-Espinoza and Fabre [9] performed numerical analyses of symmetry breakup at different surface tension values. They found that asymmetry leads to increased bubble velocity and a decreased curvature radius at the stagnation point of the bubble nose. Fabre and Figueroa-Espinoza [10] further investigated symmetry breakup experimentally and determined that asymmetry is largely independent of whether the flow regime is turbulent or laminar. They identified the vorticity-to-radius ratio at the stagnation point as a crucial parameter for symmetry breakup. Fershtman et al. [11] also studied counter-current slug flow, measuring a liquid velocity that exactly balances buoyancy $U_L = 0.35\sqrt{gD} = 0.178$ m/s, which was also observed in experiments in the present study. The latest study by Abubakar and Matar [12] provided a detailed numerical and parametric analysis of the effects of downward liquid velocity, viscosity, and surface tension on bubble shape and motion. Their linear stability analysis identified regions of dimensionless parameters where the bubble is unstable and assumes an asymmetric shape, and they explained the mechanisms behind symmetry breakup. Our experiments were conducted in the unstable region with asymmetric bubble shapes, necessitating dynamic flow rate control, as described in the following section.

The interactions between Taylor bubbles and turbulent liquid flow have been the subject of various studies. Unlike in laminar liquid flow, the tail of the bubble starts to break in the turbulent background flow. The breakup and recoalescence processes in the bubble wake region have been observed. The studies [13, 14] measured the gas loss from a stationary Taylor bubble in a counter-current liquid flow using a special spherical Teflon cap to hold the bubble in a fixed position. More recent experiments involving the turbulent counter-current regime have utilized high-speed cameras in visible light to measure the bubble's disintegration rate [15]. They have shown that disintegration by the breakup stops when the Taylor bubble is sufficiently short. This result is important for the present study focused on the Taylor bubbles, which do not lose their mass due to the breakup of the bubble's tail. As shown in [15, 37], even shorter bubbles are gradually losing their mass due to the dissolving of the gas in the liquid. However, this mechanism is much slower than the physical breakup and can be neglected over the time intervals relevant for the present study. Consequently, dynamical control of the liquid flow rate is used to trap the bubble in an equilibrium position for hours, and allowing for studies over several minutes.

Two fundamentally different approaches are used for numerical simulations of turbulent two-phase flows:

- One approach is the Euler-Euler method, wherein the Navier–Stokes equations are solved independently for each phase [16].
- Another approach is the one-fluid formulation, which involves applying a single set of governing equations across the entire domain, encompassing the interface [17]. Various methods for interface advection exist, with the Volume of Fluid (VOF) method [19, 20], Front tracking method [21], and Level-Set method [30] being among the most widely used. The present research is focused on the (VOF) method and on the Front tracking method, which were tested with the stagnant Taylor bubble in turbulent flow.

The specific version of the VOF method used in this study is implemented in the open-source OpenFOAM computer code [18]. One of the main advantages of the VOF method over alternative methods is its well-established framework and guaranteed volume conservation. Central to the VOF method is the concept of a marker function, which represents the volume fraction of one fluid within each computational cell of the domain. A key challenge in advecting a marker function is the numerical diffusion that arises from using a cell-averaged marker function [21]. To mitigate this diffusion, the VOF method reconstructs the interface so that the marker does not move into a new cell until the current cell is completely filled. Reconstruction models of the VOF method are categorized into algebraic and geometric types. Significant effort has been focused on geometric methods because they produce better results than algebraic reconstruction methods [23, 24]. One such geometric method is the piecewise linear interface calculation (PLIC) method, which has

been investigated for large eddy simulations (LES) by Kren et al. [22] and is tested in the present paper. Large eddy simulation (LES) is a very useful compromise between the high accuracy and cost of direct numerical simulation (DNS) and the lower cost but reduced accuracy of Reynolds-averaged Navier–Stokes (RANS) simulations. The development of LES methods for multiphase flows is still in its early stages, largely due to the lack of experimental and DNS benchmarks. Klein et al. [25] have laid out a framework for developing LES in multiphase flows. In single-phase flows, modeling small scales is required only for the convective term, typically achieved by adding eddy viscosity to the equations. However, multiphase flows require modeling several terms, with at least two being particularly significant. While the convective term can be approached in a similar manner to single-phase flows [26], new models are needed for other closures. Recent developments highlight that the closure of the sub-grid term for surface tension is the most critical [22].

Numerical simulations of multiphase flows using the front-tracking method have been presented by Unverdi in 1992 [27] and upgraded by Tryggvason et al. [28]. Like in the VOF method, interfacial terms are incorporated by adding the appropriate sources as delta functions at the phase boundaries. The unsteady Navier–Stokes equations are solved using a conventional finite volume or finite element method on a fixed, structured grid. The interface, or front, is explicitly tracked using connected marker points in Lagrangian coordinates, with surfaces in the 3D domain. This type of method is implemented in TrioCFD code [35], which was the second type of numerical model tested with the stagnant Taylor bubble in turbulent flow. Interfacial source terms such as surface tension are computed on the front and transferred to the fixed grid. The advection of fluid properties, like density, is handled by following the motion of the front. When large topology changes occur, the distance between marker points can increase or decrease, leading to reduced accuracy. To address this, new marker points might be added where marker density is low, and some marker points are removed where density is high. Although the method is complex to implement, it provides highly accurate tracking of the interface position. However, interface breakup does not occur well unless a special model is implemented.

Existing numerical simulations of Taylor bubbles have predominantly focused on stagnant or co-current background liquid flows across various setups, ranging from simplistic 2D and Euler-Euler simulations [31, 32] to comprehensive 3D simulations with interface tracking [33, 34]. LES investigations of Taylor bubbles within co-current turbulent regimes, without special sub-grid scale models for bubble coalescence or breakup, revealed disintegration rates one to two orders of magnitude faster than observed in experiments of Taylor bubbles within counter-current turbulent flow [22, 36].

The present study aims to address details of the Taylor bubble's interface dynamics in the region of the liquid film and the capabilities of state-of-the art numerical schemes to describe the flow of the thin liquid film and the velocity fields in the liquid and air phase around the interface. An important part of the current work is the study of interface waves: as discussed below, accurate measurements of these waves were performed despite their tiny amplitudes. Consequently, we have examined properties of the interface waves predicted by the OpenFOAM and TrioCFD codes. All instances of waves are traveling fluid oscillations sustained by the surface tension force. For experimental Taylor bubble the interface waves were studied by Kren et al. [24]. The work on the interfacial waves analysis spans beyond the films of Taylor bubbles: closely related interfacial waves are observed in vertical annular flows, where a recent review is available [39] and a more specific example by Tekavčič et. al. [38] who analyzed interfacial waves in water–air churn flow regime. Another slightly less relevant area are studies of horizontally stratified flows with the presence of capillary waves, where some of the recent activities can be found in [40, 41].

The goal of the present study is a detailed analysis of one specific experimental case performed within the experimental campaign [37], where stagnant Taylor bubbles were observed in the counter-current turbulent flow of water. The selected experimental case is reproduced with two state-of-the-art interface tracking approaches capable to operate in turbulent flow regime. Comparison of all measured parameters is performed: the main integral parameter is mass flow rate of the water that is balancing the buoyancy; flow rate is closely related to the axially asymmetric shape of the bubble, which is influencing the bubble drag. The last test is a comparison of the measured and computed interfacial waves that are traveling over the body of the Taylor bubble.

2 Experimental Setup

Experiments were conducted in a loop, as depicted in Fig. 1. The test section consisted of a 1.5 m long glass pipe with an internal diameter of D = 26 mm and wall thickness 2 mm. Water is entering the test section from the top. All experimental cases, including the one considered in the present paper, were performed in the turbulent flow regime of the liquid above the bubble, with a Reynolds number of approximately 5600. The straight section of the pipe above the bubble spanned around 40 pipe diameters, ensuring statistically uniform turbulence impinging on the bubble. To maintain a constant water temperature of 30 °C, a heat exchanger was utilized in the tank. The Taylor bubble was injected into the test section with a syringe through a small dedicated connection beneath the test section. The flow through the test section

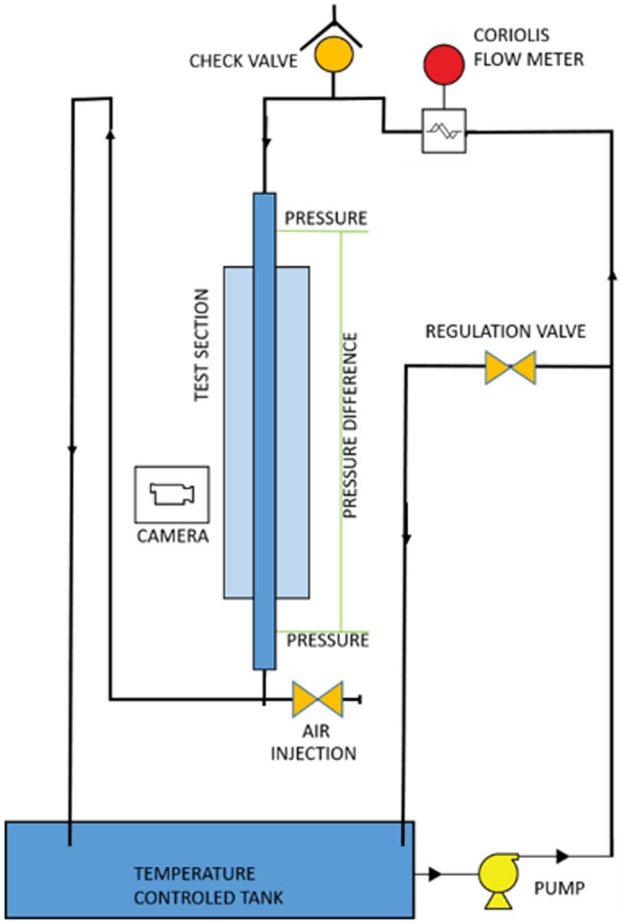

Fig. 1 Schematics of the test loop

was regulated using a control valve, which adjusted the flow distribution between the main loop and a bypass loop.

Observations of the Taylor bubble were carried out using a high-speed camera (camera Phantom v 1212, objective: TOKINA AT-X PRO D 100 mm), set up at a distance of around 30 cm between the objective and the pipe axis, with a field of view covering a 14 cm (~ 5 diameters) section of the pipe. The pipe was immersed in a rectangular glass section filled with water to minimize optical distortion. The observed Taylor bubbles typically had lengths ranging from 1.5 to 5 pipe diameters. Measurements were performed over different time intervals of 8, 4, 2, and 1 min, with camera frequencies of 100, 200, 400, and 800 Hz, respectively. Around 90 mm long bubble filmed over two minutes interval at frequency 400 Hz was used for detailed analyses in the present study.

The camera's useful resolution for the measurements was approximately 1280 × 240 pixels, corresponding to around 9 pixels per millimeter. The measurement of absolute liquid film thickness is achieved with a precision ranging between 0.5 and 1 pixel. However, this level of precision introduces relative errors exceeding 40% for very thin films below 3 pixels. The estimated optical distortion, due to the light refraction, results in a maximum enlargement of the liquid film thickness by up to 2%. This value is significantly lower than the uncertainty associated with interface reconstruction.

Each experimental run was performed in the following steps:

- Preparation of the water loop, establishment of the water circulation with an expected mass flow rate.
- Set-up of the camera, illumination, pressure, temperature and mass flow rate sensors.
- Injection of the air bubble.
- Fine-tuning of the water mass flow rate to bring the bubble into the camera's view.
- Start of measurements and active fine-tuning of the mass flow rate during the measurement.
- Data (image) processing.

In the counter-current flow configuration, the instability of the Taylor bubble requires dynamic adjustments of the mass flow rates during the experiment to ensure that the bubble remains within the camera's field of view. Minor corrections of the valve position are made every few seconds, leading to fluctuations in the bulk liquid velocity within the test section. The bulk liquid velocity is based on the readings from the Coriolis flow meter, which measures mass flow rate through the section at a frequency of 1 Hz. The variations in the mean velocity measurement due to manual mass flow rate corrections range between 3 and 10% of the bulk velocity across various experimental cases. In analysis of the results these minor changes in the bubble position were considered with a sliding coordinate system which was fixed to the tip of the Taylor bubble's nose, while the dynamics of the Taylor bubble was practically unaffected by the mass flow rate changes. As shown in [37] the bubbles moved up and down with vertical velocities below 0.01 m/s, which were considerably lower than the upstream mean liquid velocity of 0.18 m/s and the velocities around 1 m/s observed on the liquid–air interface of the bubble. While the system of bubble position control may present challenges when comparing results with similar experiments or numerical simulations, it closely resembles the numerical technique employed in high-fidelity simulations of co-current Taylor bubble flow [45, 46]. In these simulations, the Taylor bubble is modeled within a moving frame of reference to ensure the bubble remains inside the computational domain. The same approach was used in TrioCFD simulation in this paper, while the adaptive mass flow rate boundary condition was used in the OpenFOAM.

The processing of each recording involved analyzing a set of 50,000 photographs using a dedicated in-house software. The best scaling distance on the photographs turned out to be the outer diameter of the glass pipe, which is not affected by the optical distortion. This software utilized widely used libraries for tasks such as fitting two-dimensional surfaces

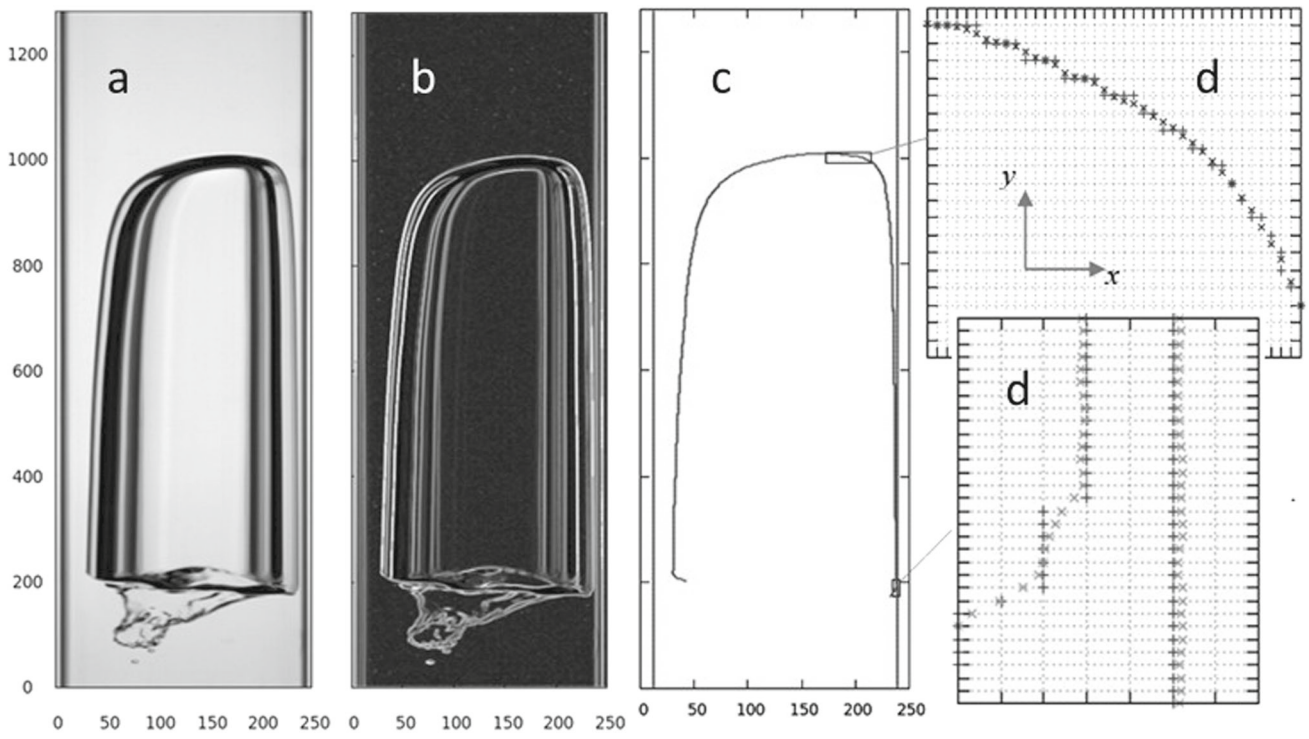

Fig. 2 **a** original image, **b** magnitude of the gradients field (step 1), **c** extracted bubble interface and pipe inner walls at pixel level (step 2), d) refinement of the interface position at subpixel level (step 3) with pixel grid in the background: " + "—pixel level interface, "x"—subpixel level interface. All units in pixels

and one-dimensional lines, performing Fourier transformations, and cross-correlating one-dimensional functions. The algorithms and techniques employed in the software were based on methods described in the Numerical Recipes book [47]. The main focus of the computer codes was image processing, specifically the extraction of the Taylor bubble surface from the images. Given the constraints of automated analysis on a large dataset, we used established image processing methods found in the open literature [48]. In order to handle the large number of photographs, manual corrections and artifact removal were limited. To address this, a robust procedure was developed that could identify potential failures in bubble interface reconstruction. A description of the algorithm can be found in [37], while the intermediate results of the particular step of silhouette reconstruction are shown in Fig. 2:

- a = > b: conversion of image density matrix into gradient matrix.
- b = > c: identification of the bubble outer surface
- c = > d: sub-pixel interface position refinement.

Distinguishing between absolute and relative accuracy is crucial when considering interface recognition. The absolute uncertainty of the interface position on a single photograph ranges from half a pixel to one pixel. However, when analyzing a time series or spatial profiles of the interface, the relative uncertainty of the interface motion between neighboring pixels in space or time is reduced by a factor of approximately 5 to around ± 0.1 pixel. This improvement in relative accuracy allows very precise characterization of interface movements.

3 Numerical methods

Modeling of the Taylor bubble in the counter-current turbulent flow was performed with two highly accurate but fundamentally rather different approaches (Table 1):

1) The Front tracking method is implemented in TrioCFD code [35]. The interface position is tracked with a Lagrangian mesh which is advected by the flow. Such an approach allows very accurate interface recognition and dynamics as the interface has a zero thickness; however, it means more expensive numerical algorithm.
2) The geometric VOF method implemented in the finite volume code OpenFOAM [22] introduces high-order interface capturing scheme, which consists of two parts—interface advection using void fraction property α and interface reconstruction with different submodels of the

Table 1 TrioCFD vs. OpenFOAM models

	TrioCFD	*OpenFOAM*
Basic scheme	Finite Element Volume	Finite Volume
Formal accuracy of discretization	2nd order in space & 3rd order in time	2nd order space & time
Interface tracking	Lagrangian front tracking	Geometric VOF (PLIC)
Turbulence modeling	quasi-DNS	LES-WALE
Inlet boundary condition	Synthetic turbulence	Recycling section
Mesh (num. of volumes/elements)	2.8 million	4.1 million
Simulated pipe length (diameters)	9	20
Taylor bubble length (diameters)	2.6	4.5

VOF method. Computing time of this approach turns out to be shorter, but slightly less accurate in modeling the interface dynamics and surface tension effects.

3.1 Front Tracking in TrioCFD

TRUST/TrioCFD is an open-source CFD code developed by the CEA (the French Atomic Energy and Alternative Energies Commission). Massively parallel, it can handle various physical situations: single or two-phase flow, chemistry, fluid–structure interaction… To model a two-phase flow, one of the possible approaches of TrioCFD is to use its front-tracking method. The latter uses an Euler–Lagrange approach coupled with a Volume-of-Fluid like method. It uses the one-fluid formulation for the fluid problem and an explicit interface tracking by considering:

- The indicator function χ_k equals 1 in the phase k and 0 otherwise,
- The variable ϕ_k (velocity, pressure, density…) having its given value in the phase k.

One can define a one-fluid variable as $\phi = \sum_k \chi_k \phi_k$. By summing the continuity equation for incompressible flows, the Navier–Stokes equation for each phase and the Laplace pressure law at the interface, one can derive the equation system:

$$div(\vec{u}) = 0$$
$$\rho \frac{\partial \vec{u}}{\partial t} + \rho\left(\vec{u}.\vec{\nabla}\right)\vec{u} = -\vec{\nabla}P + div\left[\mu\left(\vec{\nabla}\vec{u} + {}^{t}\vec{\nabla}\vec{u}\right)\right] + \rho\vec{g} + \sigma\kappa\delta_I\vec{n} \quad (1)$$

with $\overrightarrow{u}$ the velocity field, ρ the density, μ the dynamic viscosity, $\overrightarrow{g}$ the gravity field, σ the surface tension at the interface, κ the local curvature of the interface δ_I the indicator function of the interface and $\overrightarrow{n}$ the vector normal to the interface. The system of Eq. (1) is the one-fluid problem solved for the fluid mixture in the front-tracking of TrioCFD. The choice was made to use a non-conservative discrete surface tension rather than a classic Continuum Surface Force model as the latter introduces parasitic currents. The non-conservative effect has been studied and is found negligible [29].

Regarding the interface (Fig. 3), the Lagrangian mesh is advected between two time steps by the velocity field with simple advection equation applied to all Lagrangian markers on the interface $i = 1, N$:

$$\frac{d\vec{s}_i}{dt} = \vec{u}(\vec{s}_i) \quad (2)$$

where $\overrightarrow{s}_i$ denotes position of the Lagrangian marker i, and $\overrightarrow{u}(\overrightarrow{s}_i)$ represents the velocity at the marker position. To ensure the mass conservation, the transport of the phase indicator function with a calculation of the volume of gas is performed to refine the position of the Lagrangian markers. The interface treatment ends by a smoothing and a remeshing to regularize the markers position.

In this investigation, an explicit Euler scheme was used for the time integration. Regarding the space discretization, we used the Finite Element Volume method, which is a hybrid between the finite volume and the finite element methods.

As illustrated in Fig. 4 the computational domain is a vertical circular pipe with a length of L = 23 cm and a diameter corresponding to the experimental pipe. At the outlet, a free pressure condition was implemented and at the pipe wall, a no-slip condition was imposed. Fixed mass flow rate was prescribed at the inlet ($v_0 = 0.17$ m/s) and the moving frame of reference approach was used in TrioCFD simulation.

As the inlet flow is turbulent, a synthetic turbulence developing an isotropic and homogeneous turbulence was chosen as a boundary condition. The values of turbulent kinetic energy k and turbulent dissipation rate ε on inlet were computed with a preliminary RANS standard k-ε computation. Even though this does not exactly mimic the conditions in a pipe, this approach combined with a certain development length above the bubble head provides satisfactory results and a reasonable computational cost. Let us note that this branching between the synthetic turbulence and the two-phase domain significantly increases the computational time compared to simulations of Taylor bubbles performed with a laminar inlet condition showing excellent results [42]. Future development to optimize the process is ongoing.

The bubble is initiated as a hemisphere at the head, contiguous to a cylinder of a same radius letting a liquid film of a

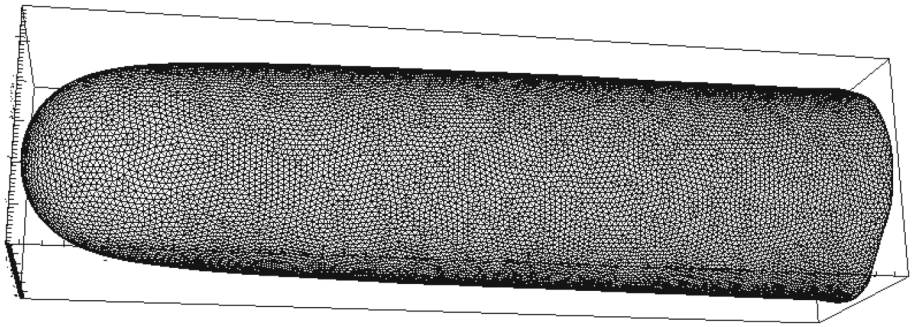

Fig. 3 Illustration of the Lagrangian mesh tracking the interface in TrioCFD

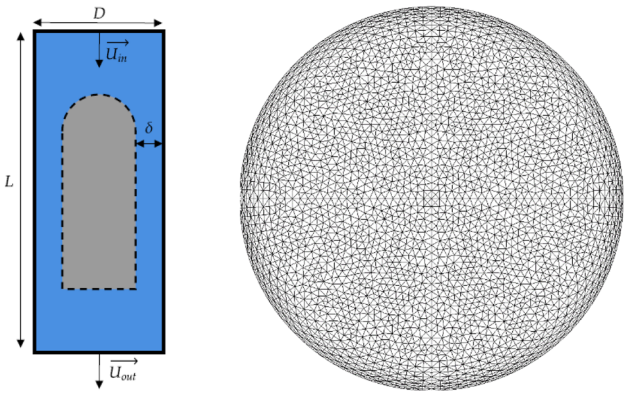

Fig. 4 Left: scheme of the computational model. Right: cross section of the mesh

thickness δ chosen as 2.6 mm (10% of the diameter). This is significantly thicker than the final film thickness but it eases the initialization of the computation. To avoid the bubble to break during the initialization because of the fluid forces, two techniques were used:

- The surface tension of the bubble was initiated with a value ten times higher than the physical one, then linearly decreased to its physical value during 0.1 s.
- Three zones of uniform velocity were set to avoid excessive initial fluid force: no velocity in the bubble, higher velocity around the bubble, and nominal velocity in the rest of the domain.

The computational domain was meshed using the internal mesh generator of TRUST/TrioCFD coupled with GMSH. The process starts with meshing a quarter of disk in two different sections:

- a corona filled with prisms whose size follows a geometrical expansion law. The latter are then cut to triangles.
- the bulk domain homogeneously filled with triangles.

The resulted mesh is then extended to generate the mesh of the circular cross section (see Fig. 4) and then extruded to produce the entire pipe. The final mesh for TrioCFD simulation constituted of about 2.8 million tetrahedral elements. Details of the mesh characteristics can be found in Table 2, η being the Kolmogorov length scale computed as $\eta = \nu^{3/4}\varepsilon^{-1/4}$ with ν the liquid kinematic viscosity and ε the turbulent dissipation rate, itself estimated with the turbulent length scale approach. The subgrid turbulent model was not used, which means that the code worked with a so-called quasi-DNS approach: mesh was too coarse for DNS but sufficiently fine to allow simulations without turbulent diffusivity.

The length of the bubble after the initial non-physical interval of 0.1 s, was established at around 70 mm. Time interval of the observation was 1 s and the computation took 45,000 CPU-hours on 128 CPU cores.

3.2 Geometric VOF interface tracking in OpenFOAM

A two-phase gas–liquid system has been modeled using the one-fluid formulation of the Navier–Stokes Eqs. (1) and the geometric VOF approach for interface capturing. Within the VOF framework, a void fraction, denoted as α, is defined. Its advection equation is given as:

$$\frac{\partial \alpha}{\partial t} + \alpha \boldsymbol{u} \nabla \alpha = 0. \tag{3}$$

Solution of this equation represents the starting point for the VOF reconstruction of the interface. It is important to emphasize that interface treatment with Lagrangian markers in Eq. (2) and through the volume fraction advection Eq. (3) is the key difference between both numerical models used in the present study.

In this computational study, the OpenFOAM v10 software, a widely recognized tool in the field of computational fluid dynamics (CFD), is employed to solve the relevant equations. The core of the simulation is a highly sophisticated and modified interFoam solver. This solver is notable for its capability to utilize diagonally implicit Runge–Kutta (DIRK) time integration schemes, seamlessly integrated with the piecewise linear interface calculation (PLIC) for geometric reconstruction of interfaces. This solver is an advanced iteration of an

Table 2 Characteristic sizes of the mesh

Bulk Δx [mm]	Bulk Δz [mm]	Bulk Δx/η [−]	Bulk Δz/η [−]	Wall y^+ [−]
0.5	1.4	4	12	1.5

original version developed in OpenFOAM v4 by Frederix et al. [45], which was later refined by Kren et al. [22].

For modeling the subgrid-scale phenomena, the study adopts the Wall-Adapting Local Eddy-viscosity (WALE) model. This eddy viscosity model is particularly effective in capturing the dynamics of turbulent flows at smaller scales. The computational strategy includes the use of the Pressure-Implicit with Splitting of Operators (PISO) algorithm. This algorithm plays a pivotal role in the computational process, as it adeptly decouples the pressure and velocity equations, allowing for their segregated solution. A notable feature of this methodology is the incorporation of two inner corrector loops. This design implies that the pressure equation is reformulated and resolved twice within each stage of the Runge–Kutta (RK) time-stepping process.

Surface tension, a crucial aspect in multi-phase flow simulations, is computed using the continuum surface force (CSF) model [51]. This model effectively distributes the surface tension force across several computational cells, utilizing a Dirac delta function. To enhance the accuracy of this approach, the Dirac-delta function in the surface tension term is smoothened via the α function. The primary objective of this modeling technique is to precisely equilibrate the forces due to pressure gradients and surface tension, ensuring accurate representation of the physical phenomena in the simulated fluid system. For the spatial discretization of the divergence terms, the finite volume framework was used, which eventually reduces to a simple summation of all the face-normal fluxes across all the faces enclosing each control volume. Similarly to Kren et al. [22], a blended scheme was used for momentum convection term that stabilizes the artificial breakup and does not have a detrimental effect on the single-phase turbulence far away from the bubble. All other interpolations and gradients are discretized using linear schemes, which are second-order accurate. The modified solver is able to use any Runge– Kutta scheme. In the present computation, a Diagonally Implicit Runge–Kutta scheme of second order (DIRK2) was used with the CFL number in the simulations below 0.4.

To simulate a Taylor bubble in a counter-current flow under turbulent conditions, a recycling boundary condition was used at the inlet, situated upstream from the Taylor bubble. This recycling process occurs five hydraulic diameters (D) from the inlet, allowing sufficient space for the velocity field to develop fully. Beyond the recycling point, a distance of two to three diameters is maintained before the Taylor bubble's nose, ensuring it doesn't affect the boundary condition. The flow rate is continuously adjusted at each time step to balance the bubble's buoyancy against hydrodynamic drag, keeping the bubble's position relatively stable in the simulation. This method is depicted in Fig. 5. To counter minor fluctuations, a gentle relaxation factor of 0.01 was employed, ensuring the bubble remains steady.

The OpenFOAM model described above was successfully used for simulation of a stagnant Taylor bubble in the counter-current water flow in a thinner pipe at Re = 1400 [22]. These results were compared with experiments performed under the same conditions. The Re = 1400 case represents laminar flow of water above the bubble, laminar flow in the liquid film and chaotic flow with developing turbulence under the tail of the bubble. The model successfully described the laminar region of the water flow and the turbulent region under the tail of the Taylor bubble. The laminar-turbulent case at Re = 1400, where bubble retains axial symmetry, was a starting point for the present, fully turbulent model at Re = 5600, and the corresponding mesh density.

In the present investigation, characterized by a Reynolds number of 5600, three distinct mesh resolutions were used, all of them prepared with "Salome Meca" tool [49], with two of them depicted in Fig. 6. Each mesh shared an identical cylindrical shape, with a length of 0.52 m and a diameter of 26 mm. The G30 mesh consisted of around 700,000 hexahedral cells and the G15 mesh was composed of about 4.1 million cells. The naming convention of the meshes corresponds to the dimensionless spanwise cell size in the bulk flow.

Near the wall regions, the spanwise cell size was maintained at less than one wall unit. This wall unit, denoted as dx^+, is defined by the formula $dx^+ = dxU/\nu$, where dx represents the cell width in actual units, U signifies the friction velocity, and ν is the kinematic viscosity. Along the streamwise direction, the cell sizes were generally kept comparable to those in the spanwise direction, albeit with additional refinement in the vicinity of the bubble.

The OpenFOAM set-up described in this section was used and verified in simulations of Taylor bubble flow in Kren et al. [22], where laminar liquid flow at Re = 1400 was prescribed at the inlet. The problem considered in [22] had simpler nature of the flow at the Taylor bubble's body, but more complex tail behavior than in the present work: Taylor bubble in [22] was longer and experienced break-up of tiny bubbles at the flapping tail, where laminar to turbulent transition occurred. In the present work, the liquid flow is fully turbulent everywhere, but the bubble is shorter and does not

Fig. 5 Schematic of recycling boundary condition inside the computational domain (note the direction of the gravity)

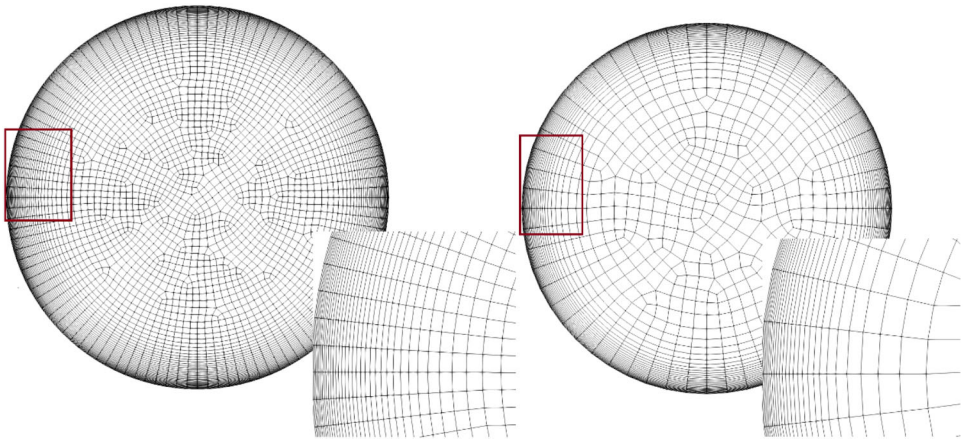

Fig. 6 Mesh G15 (left), G30 (right)

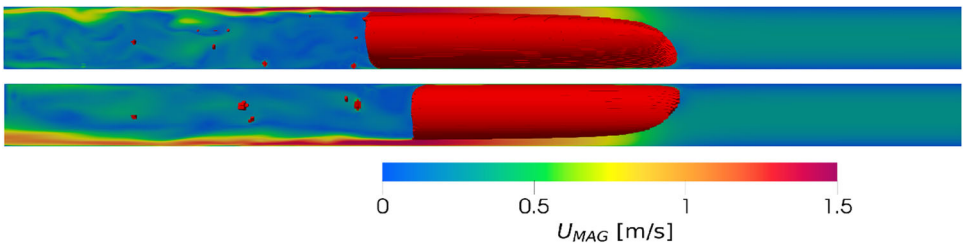

Fig. 7 Comparison of instantaneous liquid velocity magnitude fields on G15 (fine—top) and G30 (coarse—bottom) mesh. Bright red denotes air phase. Both drawings are given at the same time t = 10 s in the simulation

exhibit a significant break-up. The intensity of the bubble breakup was actually the most important parameter that was affected by the mesh density as shown in Fig. 7; coarser mesh (G30) bubble has lost larger amount of mass in the same time interval in comparison with the finer mesh (G15). Further comparison of grid sensitivity study shown in Fig. 7 shows different azimuthal orientation of both bubbles, which is randomly established very early in the simulations. Other properties of the Taylor bubble, like the mean mass flow rate and shape of the nose, were rather similar on both meshes. Consequently, only the fine mesh (G15) results are presented in the next sections.

The length of the bubble in the OpenFOAM simulation was around 120 mm. Time interval of the simulation was 12 s, which took 110,000 h of CPU time on 192 computer cores.

4 Results

In this section, we compare one experimental and two simulated bubbles with their main properties collected in Table 3. One can see that the bubbles are of different length. This was not planned: the initial intention was to have bubbles of the same length in both simulations performed by both groups of researchers. When it was found that bubbles in TrioCFD and OpenFOAM simulations have different lengths, both simulations were running already for a month and a decision was made to continue without changing the length. The decision was based on experimental results described in [37], which have shown that for the bubbles of the length between two and six diameters, the main properties, like the bubble velocity, shape, and water mass flow rate, do not depend on the length.

As demonstrated in [37] time-averaged bubble shape is not axisymmetric. Instead the bubble exhibits a quasi-stable asymmetric shape: the bubble is always inclined toward one side of the pipe wall. The azimuthal direction of the inclination is determined during the injection of the bubble. As discussed in [37], this behavior did not allow predictions of the time-averaged 3D shape of the Taylor bubble in turbulent counter-current flow based on the 2D shadowgraphy measurements. This asymmetry of the bubble can be easily analyzed in 3D simulations, in the 2D photographs however,

Table 3 Properties of the Taylor bubbles in experiment and simulations (* value for symmetric bubble)

	Length [mm]	Time of observation (s)	Initialization transient time (s)	Steady-state time (s)	Steady-state mass flow rate normalized to experiment ($v_0 = 0.179$ m/s)
Experiment	90	125	/	/	1
TrioCFD	70	1.7	0.2	/	0.75*
OpenFOAM	120	12	0.2	3–5	1.17

it is important to perform measurements in the plane, where the bubble asymmetry is maximal. Out of around 10 different experimental cases, where asymmetry was observed at different azimuthal angles, we have selected one with the most pronounced asymmetry in the camera's field-of-view. Even this case is not exactly perpendicular to the 2D plane of the photograph; however, it is sufficiently close and is chosen as a representative case in the present paper.

The second important parameter for comparison of the Taylor bubbles is the time interval of the observation. Our experience shows that it is ideal to have a time interval of around one minute. As seen in Table 3, such time intervals were not achievable in simulations due to the high computational costs and/or large numerically induced breakup of the bubble.

When time interval is considered, the influence of the initial conditions in the simulations must be emphasized: both simulations start with symmetric and non-physical shape of the bubble, which is followed by a rather vigorous semi-physical transient. Consequently, a short time interval of a couple of tenths of a second must be neglected in analyses of the results. The second characteristic time in the simulations is the time interval where the initial symmetry of the bubble is broken and a quasi-stable asymmetric bubble shape is obtained. In OpenFOAM simulation the asymmetry was established after 3–5 s. After that time, the comparison of the bubble shape in experiments and simulations is feasible and the total drag of the bubbles can be compared.

As seen in SubSect. 4.1 and in Table 3, attaining the proper steady-state bubble shape, which is ultimately responsible for the bubble's drag, was a challenge in OpenFOAM simulation. The ultimate bubble shape predicted by the OpenFOAM had lower drag than the actual experimental bubble. Consequently, 17% higher mass flow rate was needed to keep the bubble stagnant in simulation (Table 3).

In the TrioCFD simulation, a fixed mass flow rate (mean water velocity $v_0 = 0.18$ m/s) and a moving frame of reference were used to keep the bubble in place. Since the TrioCFD simulation did not achieve the steady-state asymmetric shape, the bubble experienced stronger drag force and was moving down with velocity around 0.04 m/s. This motion was compensated with the moving frame of reference. As a rough estimate, the mean downward velocity of water, which would keep the symmetric bubble stagnant, would be around 0.13 m/s. This is about 75% of the measured downward velocity (Table 3).

4.1 Taylor Bubble Shape

Typical instantaneous shapes and sizes of the bubbles taken at times several seconds apart are shown in Fig. 8, while Fig. 9 shows time-averaged bubble shapes. In the OpenFOAM simulation, the interface was defined as an isoline with values of the gas (and liquid) volume fraction equal to 0.5. In TrioCFD this definition is not needed: exact position of the interface markers is available at any time. Time averaging in the experiment was performed over a 2-min interval. In the OpenFOAM simulation, time averaging was performed in the interval from 6 to 12 s, where the bubble lost the symmetry imposed by the initial conditions and developed a roughly steady-state asymmetric shape. In the TrioCFD simulation, the analyzed time interval was only 1 s long and that was not enough for development of the asymmetric shape. Consequently, instantaneous TrioCFD bubble is the same as the time-averaged bubble, only one profile is given in Fig. 8, and there is no TrioCFD profile in Fig. 9.

Time averaging takes into account slow vertical motion of the Taylor bubble in experiment and in simulations. The time-averaged bubble shapes in Fig. 9 are obtained in a moving frame of reference: origin of the coordinate system in axial direction is attached to the axial position of the bubble nose tip at every instantaneous snapshot before averaging.

The time-averaged measured bubble in Fig. 9 is inclined to the right side of the image; however, one of the three instantaneous profiles in Fig. 8 shows a bubble inclined slightly to the left. One can also note that the tail of the bubble is not resolved in all instantaneous experimental cases. The dynamics of the bottom surface is a strong 3D phenomenon, and capturing the tail position from 2D shadowgraphy does not give a particularly useful information. Consequently, the software for interface identification was not forced to work in this region.

Three instantaneous shapes of the bubble from OpenFOAM simulation are given in five seconds intervals in Fig. 8,

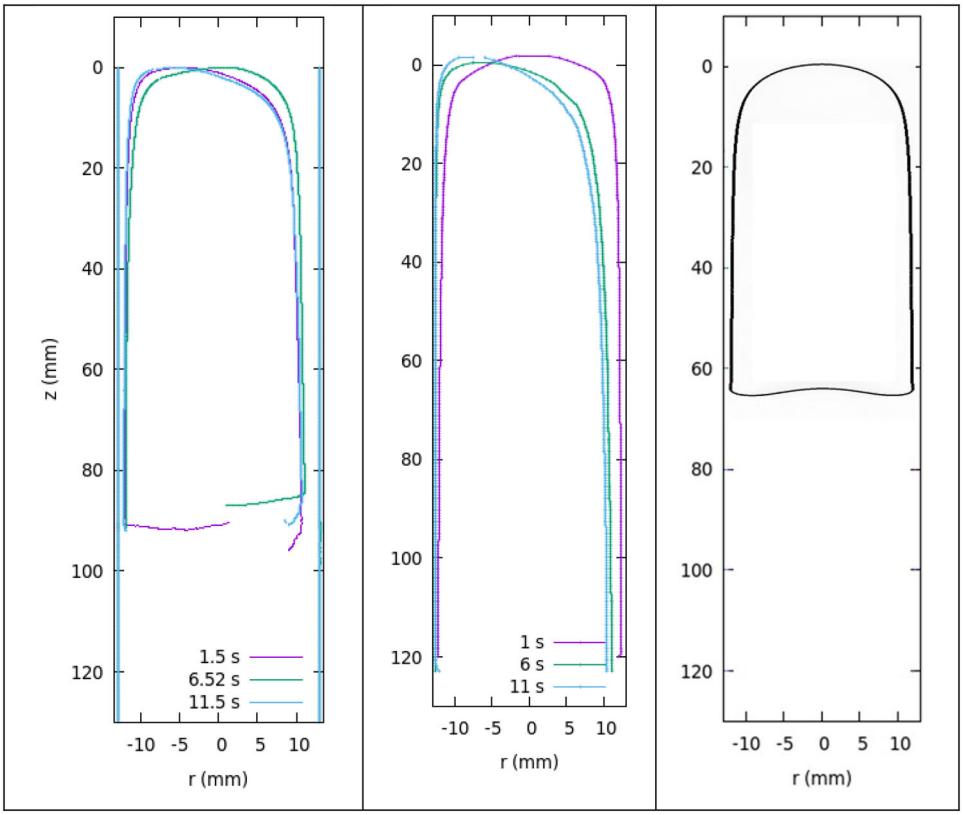

Fig. 8 Instantaneous silhouettes of measured Taylor bubble (left), OpenFOAM simulation (center), and TrioCFD simulation (right). Pipe walls are drawn in experimental image. Walls in simulations are left–right edges of the image

center: the first silhouette shown 1 s after the start of simulation is showing nearly symmetric bubble, which has not achieved the quasi-steady asymmetric shape yet. Symmetry is broken and developed at times 6 s and 11 s. These two silhouettes exhibit higher asymmetry than their experimental counterparts. Consequently, such a shape of the bubble exhibits lower drag and requires a higher mass flow rate for dynamical balance, as reflected in Table 3.

As seen from the experimental silhouettes in Fig. 8 the bubble's nose occasionally crosses the axis; however, on average, it remains attached to the same azimuthal angle of the pipe throughout the several minute time interval. This phenomenon is further demonstrated in Fig. 10: 12 s time interval allows direct comparison with the OpenFOAM simulation. Wobbling of the nose is stronger in the experiment and less intensive in the OpenFOAM simulation. The important information from Fig. 10 is more intensive fluctuations of the experimental bubble in comparison with the simulated bubble from OpenFOAM simulation. This is a clear sign that the existing OpenFOAM model cannot provide a perfect description of the phenomena.

Transition from symmetric OpenFOAM bubble to quasi-stable asymmetric one is also rather clearly seen in Fig. 10. The simulations started with an axially symmetric Taylor bubble, and the bubble nose position has moved to the wall in about three to five seconds. After that the bubble nose stays close to the wall and the final asymmetry of OpenFOAM bubble is much more pronounced than in the measurements.

Deviations from the experiment are not without consequences: next to the higher liquid mass flow rate needed to counter-balance the OpenFOAM bubble given in Table 3, simulated bubble creates a very thin liquid film seen on the right side of the 2D image in Fig. 9 (center). The film eventually becomes so thin that it ruptures and the air comes into the direct contact with the pipe wall. This phenomenon does not have a physical background since it was never observed in experiments. Consequently, the simulations are stopped at such instances and subgrid models of interface friction and surface tension are being investigated to improve that behavior.

The asymmetry in the bubble of the TrioCFD simulation was not achieved in the observed time interval, thus its long-time behavior cannot be predicted at this point. Nonetheless, during that time frame, radial motion of the bubble nose was observed, but it was not relevant to compare as it was only about one percent of the pipe diameter. The axial velocity of the TrioCFD bubble was 0.04 m/s downward and this was taken into account in Table 3 mass flow rate ratio calculation. This seemingly larger difference is due to the higher drag coefficient of the symmetric bubble compared to the asymmetric one. This ratio cannot be used to extrapolate the

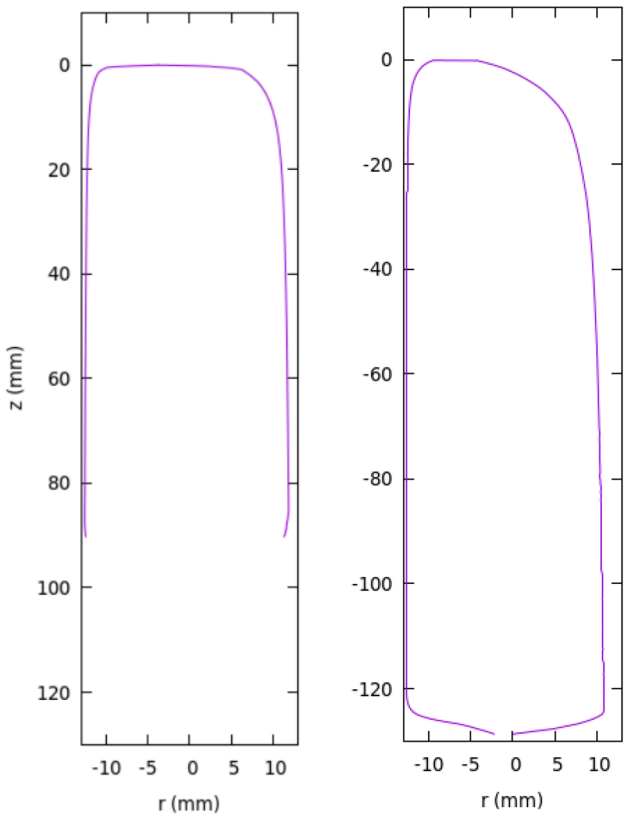

Fig. 9 Time-averaged Taylor bubble interface position: experiment—2 min time interval (left), OpenFOAM average Taylor bubble position over 6 to 12 s time interval (right)

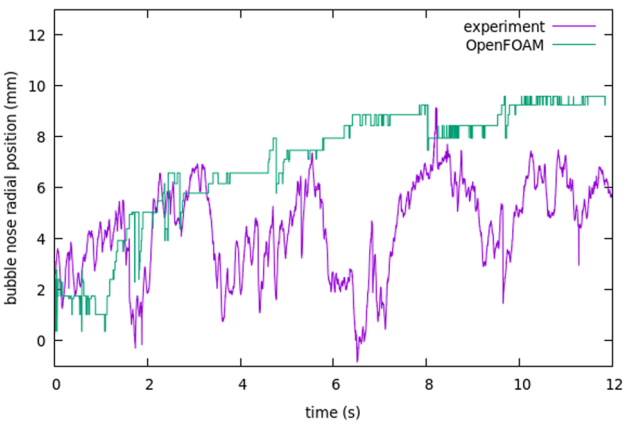

Fig. 10 Radial position of Taylor bubble's nose

final mass flow rate that would balance the TrioCFD bubble once the quasi-stable asymmetric shape is reached.

4.2 Liquid Film Thickness and Interface Axial Velocity

The asymmetry observed in the time-averaged Taylor bubble, as depicted in Sect. 4.1, presents challenges when it comes to independently verifying our measurements. However, a way to mitigate this issue was averaging the bubble shape and corresponding liquid film thickness over both sides of the photographs. These findings are presented in Fig. 11, which illustrates the liquid film thickness along the bubble. The axial distances along the z-axis of Fig. 11 are measured from the bubble nose. Solid lines represent the time-averaged and left–right spatial averaged profile derived from the measurements and simulations. Dashed lines represent time-averaged left and right (thick and thin film) profiles separately, i.e., magnification of the near-wall region in Fig. 9. The magnification of the film thickness in Fig. 11 shows that the average thickness is very similar in experiment and OpenFOAM simulation. Figure 11 is clearly exposing the feature mentioned above: bubble asymmetry is more pronounced in OpenFOAM simulation than in the experiment and the difference between the thick and thin film side is larger in OpenFOAM simulation.

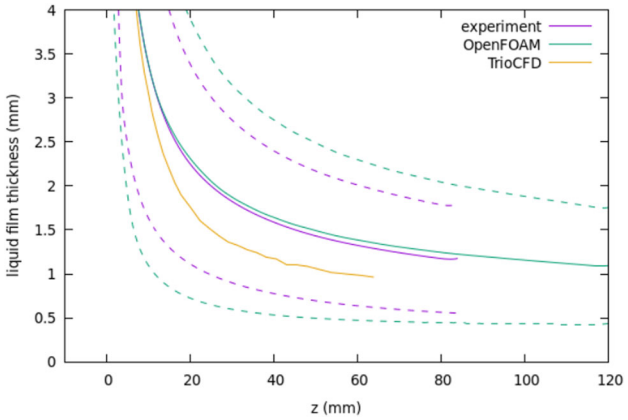

Fig. 11 Average liquid film thickness: solid lines. Dashed lines: thick and thin films. Measurement uncertainty is below 0.1 mm and is not plotted

The approximately 25% thinner film in TrioCFD simulation is due to the lower drag of the symmetric bubble, which is proportional to the reduced effective mass flow rate (effective mass flow rate is equal to imposed mass flow rate minus moving frame of reference contribution). Since the thick and thin films in TrioCFD are equal to the average, only one profile is shown in Fig. 11.

By utilizing the averaged film thickness profiles from the measurements, an additional curve related to the mean downward liquid velocity in the film region can be derived. Based on the continuity equation and known upstream liquid velocity v_0 (0.179 m/s), the mean liquid velocity can be calculated as $v(z) = v_0 R^2/[2Rh(z) - h(z)^2]$, where R represents the pipe radius (13 mm) and $h(z)$ represents the liquid film thickness at a given axial position z. By assuming the measured film thickness, one can calculate the mean liquid velocity within the film region. However, the quantity of interest is

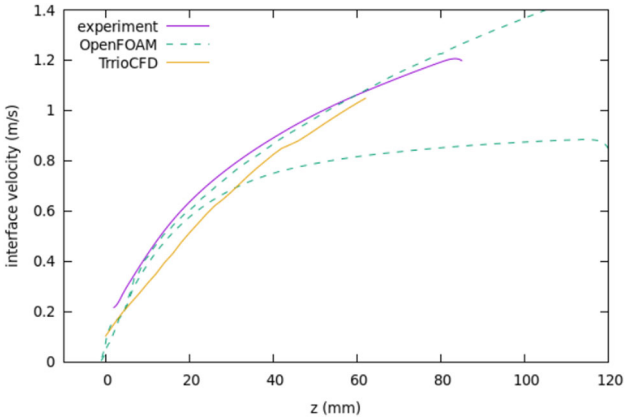

Fig. 12 Taylor bubble interface velocity (m/s): OpenFOAM and TrioCFD—obtained directly from simulations. Experiment—obtained from film thickness and continuity equation. OpenFOAM: left and right interface velocity

interface velocity and with the presented measurement techniques it cannot be measured. Nevertheless, a reasonably good approximation is available: the velocity of the interface can be estimated from the mean liquid velocity based on the liquid film thickness. The interface velocity was obtained from the mean liquid film velocity by multiplication with a factor of 1.15. This semi-empirical factor stems from the DNS simulations of the turbulent flume [50] and contains relative error around 2–3% [37]. It applies to the fully developed free liquid surface near an infinite flat wall and disregards the air shear force. As shown in [37], this approximation can be used, because the interface velocity is very similar on all sides of the bubble and does not depend on the thickness of the liquid film.

In simulations, the interface velocity can be obtained directly from the data. In the OpenFOAM results, the interface velocity is defined as a velocity at the isoline with the values of the gas (and liquid) volume fraction equal to 0.5. In the TrioCFD results, this velocity is directly obtained as a velocity of the Lagrangian marker points on the interface.

Figure 12 presents the experimental interface velocity profile for the time-averaged and spatially left–right averaged film and interface velocities from simulations. The relative uncertainty of the measured time-averaged velocity profile is similar in magnitude to the uncertainty of the mean film thickness measurement, approximately 10% at distances greater one diameter D from the bubble nose.

Numerical interface velocity profiles in Fig. 12 can be easily extracted for each side of the Taylor bubble separately and are also plotted separately for OpenFOAM simulation. Only one profile is given for TrioCFD simulation in Fig. 12 due to the symmetry of the bubble.

As further explained in [37] and in Sect. 4.3, where interface velocity is analyzed with a different approach, very similar interface velocities are expected on both sides of the Taylor bubble. Nevertheless, the OpenFOAM simulation shows very good agreement of the interface velocity only on the thick side of the liquid film. Significantly slower interface velocity is observed in the region of the thin film. Mesh resolution in OpenFOAM G15 mesh simulation describes 0.5 mm liquid film with around 10 mesh points in radial direction. This is actually coarse for an accurate description of a turbulent film with LES. If we add that the interface is smeared over 2 to 3 points, we can conclude that the higher radial resolution or a more elaborated subgrid model is needed around such interface.

The velocity profile of the TrioCFD simulation is close to the measurements and within the uncertainty of the measurements, which are characterized with a single uncertainty bar at around $z = 70$ mm. It is clear that the markers are accurate in specifying the location and the velocity of the interface. Nevertheless, the high similarity between the TrioCFD and measured interface velocities is due to the fact that the walls in the TrioCFD simulation are moving up at around 0.04 m/s along with the moving frame of reference, while the bubble is fixed in space.

4.3 Axial Velocities of Disturbance Waves on the Interface

The presented measurement techniques and image processing algorithms allow us to track small disturbance waves traveling along the Taylor bubble interface [43, 44]. This technique was used and described by Kren et al. [37]. The specific mechanisms generating these waves are not entirely clear, but the waves are believed to be induced by the turbulence. However, assuming that most of the waves are produced by random disturbances, they are expected to travel in all directions parallel to the air–water interface. The velocities of these waves are governed by the capillary wave equations, as described in [5]. The dispersion relation of capillary waves can be expressed as:

$\omega^2 = \frac{\sigma k^3}{\rho} \tanh(kd)$,

where $k = 2\pi/\lambda$ is the wavenumber, $\omega = 2\pi\nu$ angular frequency, and $c = \lambda\nu$ is the phase velocity. For typical "thick" 2 mm liquid film waves, the characteristic frequencies, wavelengths, and phase velocities are approximately 1 Hz, 50 mm, and 0.05 m/s, respectively. For the thinner 0.5 mm liquid film, these values are approximately 40 Hz, 5 mm, and 0.2 m/s. These estimates indicate that the characteristic phase velocities of the waves are lower than the interface velocities shown in Fig. 12, implying that practically all waves on the interface travel downward.

To estimate the axial velocities of the disturbance waves traveling over the interface, measurements of the axial

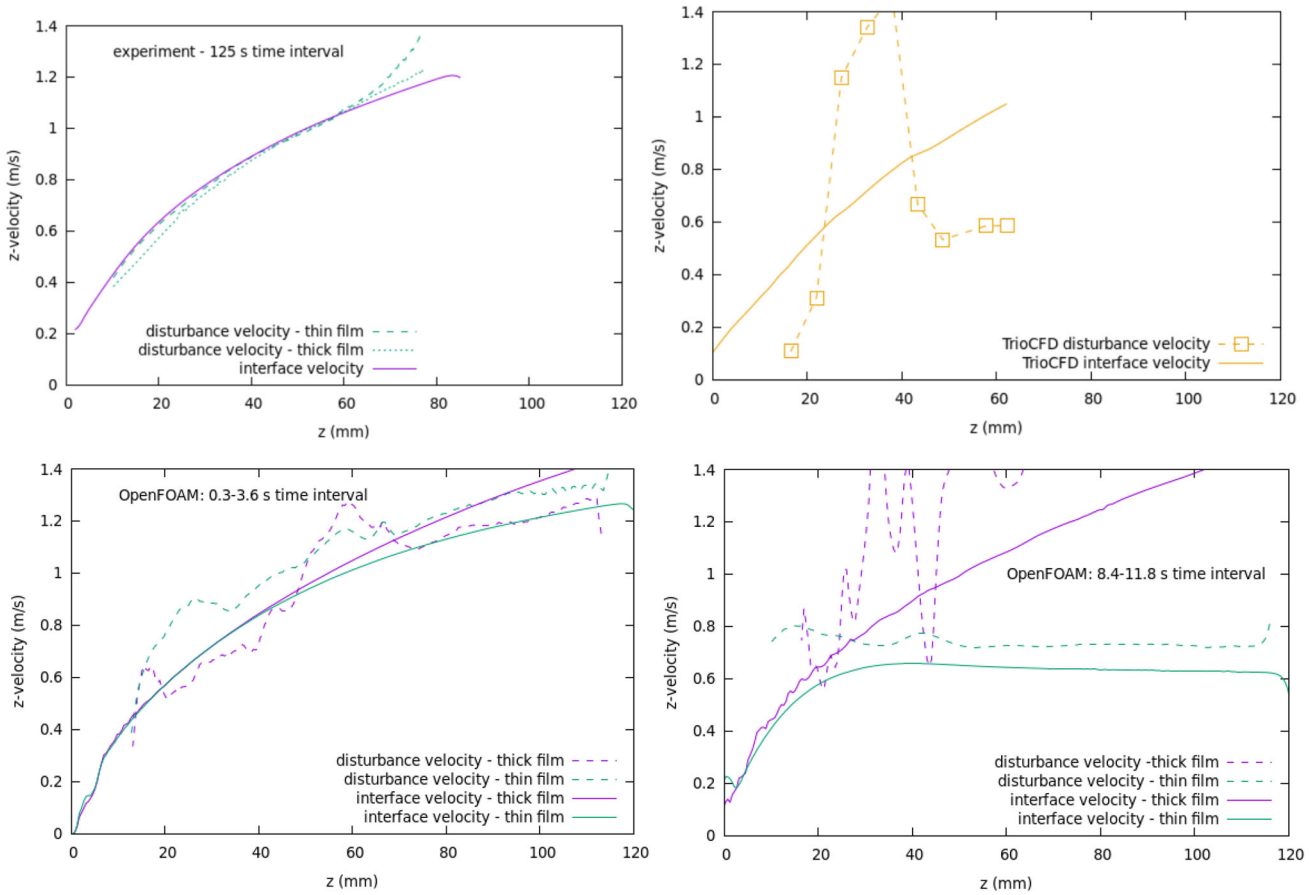

Fig. 13 Disturbance velocity (dashed) vs. interface velocity (solid) in the experiment (top-left), TrioCFD (top-right), and OpenFOAM (bottom-left [0.3 s:3.6 s] interval and bottom-right [8.4 s:11.8 s] interval)

disturbance wave velocity w are performed using cross-correlations of the time signals at various axial positions along the pipe. By selecting a distance H between specific points in space, for example, $H = 200$ pixels, the velocity w can be obtained from the measured time lag τ of the signals as $w = H/\tau$. For example, the time lag at the point 400 pixels downstream of the bubble nose and at a distance $H = 200$ pixels, is computed from the cross-correlation of time signals at points $400 - H/2 = 300$ pixels and $400 + H/2 = 500$ pixels. The procedure is described in [37], where it was applied to the measurements.

The same procedure was used also for analyses of the disturbance wave velocities in the OpenFOAM simulation results and the results are presented in Fig. 13 together with the interface velocities. Velocities are given for one real and two simulated Taylor bubbles listed in Table 3. The disturbance wave speed profiles are derived from the time lags observed in the right-hand side of the silhouettes, except for TrioCFD results, where both sides are symmetric and the results are very similar and not repeated twice.

The complete time history consisting of 50,000 frames over 125 s interval is analyzed for measurement. In the OpenFOAM results two intervals of the same length 3.4 s at the beginning and at the end of simulation (50–2050 frames and 5000–7000 out of total 7000 frames) were used. In the TrioCFD simulation around 1700 frames were analyzed over a 1.7 s interval. Cross-correlations are compared at a fixed distance of around 11 mm in measurements and in OpenFOAM, and 20 mm in TrioCFD. The discrete values of cross-correlation time lags are smoothed using parabolic interpolation.

Figure 13 shows disturbance velocities and the corresponding interface velocities in experiment and in simulations. They are separated into four separated graphs plotted on the same spatial scale and with the same velocity range in order to make the differences and similarities clear. Both distinct types of velocity profiles are obtained from the same measurements but through entirely different analysis. The interface velocities are obtained directly from the simulations and from the measurement of the liquid film thickness in the experiment. On the other hand, the disturbance velocities are determined based on the relative motions of the

liquid–air interface. Notably, both types of velocities exhibit remarkable similarity in most of the graphs in Fig. 13. This observation confirms the hypothesis given in [37] that the time-averaged velocity of the disturbance waves on the water–air interface effectively represents the velocity of the interface itself.

Before proceeding to the further discussion it is important to address the discrepancies seen in the graphs of Fig. 13. Disturbance velocity profiles obtained in experiment show very similar disturbance wave velocities on both sides of the photograph, despite significant difference in the liquid film thickness seen in Fig. 8 and in Fig. 11. Similar observation was reported in other experimental cases in [37]. Further observation of experimental profiles shows increasing discrepancies on the right side of the photographs in the region beyond 70 mm from the bubble's nose. This discrepancy appears in the region of poorer spatial resolution in the thin film, which is resolved on 2–5 pixels. Very thin liquid film filters the long wavelengths, which are the most relevant for accurate evaluation of the disturbance velocity measurements. Short wavelengths, which remain on the thin films, are more difficult to resolve with the limited resolution of the presented experiment. The only solution is to increase the spatial resolution of the photographs.

The disturbance velocities in TrioCFD were obtained in 8 points along the bubble, which are marked with symbols in Fig. 13. Computation of cross-correlation functions is difficult and sensitive to the noise even on the fixed meshes of the photographs and OpenFOAM results. The problem becomes even more difficult for TrioCFD, where cross-correlation functions must be obtained from the moving markers on the interface. Consequently, for the given spatial resolution, only very rough estimates of disturbance velocities are available in TrioCFD (Fig. 13).

Lastly, we need to comment on the disturbance wave velocities computed from the OpenFOAM results using the same procedure as in the experiment. Two separate graphs are shown in Fig. 13 for OpenFOAM, one for the interval at the beginning of the simulation during the time interval [0.3 s: 3.6 s] where the bubble is losing its symmetry, and the other for the time interval [8.4 s: 11.9 s] where the bubble is close to quasi-steady-state and with a very thin liquid film on the left side plane shown in Fig. 8. Disturbance velocity profiles computed in the first time interval where the Taylor bubble is close symmetric are not smooth, but reasonably close to the computed interface velocities. Coarse, ~ 0.05 mm, radial resolution in the near wall region can only provide a very rough approximations of the disturbances with amplitudes 0.01–0.05 mm.

The problem is more exaggerated in the time interval at the end of the OpenFOAM simulation. At that time, the liquid film becomes very thin on one side and rather thick on the other side. As shown in Fig. 13 the cross-correlation technique still works for the thin film (not with a great precision), but fails on the thick side. The reason for this failure is film position, which is not within the finely resolved boundary layer visible in G15 mesh of Fig. 6, but in the coarser central region where small disturbance waves cannot be captured anymore.

The equivalence between the time-averaged velocities of the interface waves and the convective velocity of the interface observed in experiments, is thus roughly confirmed also in simulations. The main reason for the equivalence lies in the fact that the characteristic velocities of the dominant disturbance waves are significantly lower, at least by an order of magnitude, compared to the mean velocities of the liquid film (approximately 1 m/s). As a result, the time averaging process predicts the final disturbance wave velocity equal to the time-averaged convective velocity of the water–air interface.

The final comparison of the experiment and simulations is focused on spectra of the disturbance waves traveling in the axial direction over the body of the Taylor bubble. Figure 14 shows power spectra of the disturbance waves analyzed in a point approximately 50 mm below the Taylor bubble's nose. The common property of measured and TrioCFD spectra is very sharp drop at frequencies above 10–20 Hz. An exception is seen in the OpenFOAM results and we assume that the difference is due to the implemented numerical scheme in combination with the LES-WALE mode, which does not sufficiently suppress the fluctuations in the range of frequencies between 10 and 70 Hz.

The highest frequencies of the turbulent fluctuations in the single-phase flow of water above the bubble can be estimated from the DNS database of Kasagi (Fukata and Kasagi, 2002) pipe flow case at $Re = 5300$, which is close to the present experimental conditions. Their highest frequencies of Kolmogorov scale vortices are between 10 and 70 Hz in the axis of the pipe and in the near-wall region, respectively. Since the turbulent kinetic energy in the vortices at the Kolmogorov scales is low, frequencies between 3 and 20 Hz, which correspond to the Taylor microscales, seem to be more relevant as the upper limits.

Spectral analysis of the waves traveling over the Taylor bubble's body shown in Fig. 14 is representative also at other distances from the bubble's nose.

5 Conclusions

This paper summarizes the studies of the Taylor bubble in a vertical turbulent counter-current air–water flow, excluding the bubble's tail region. The analyses are based on results available from high-precision 2D shadowgraphy observations which are compared with high-fidelity simulations with

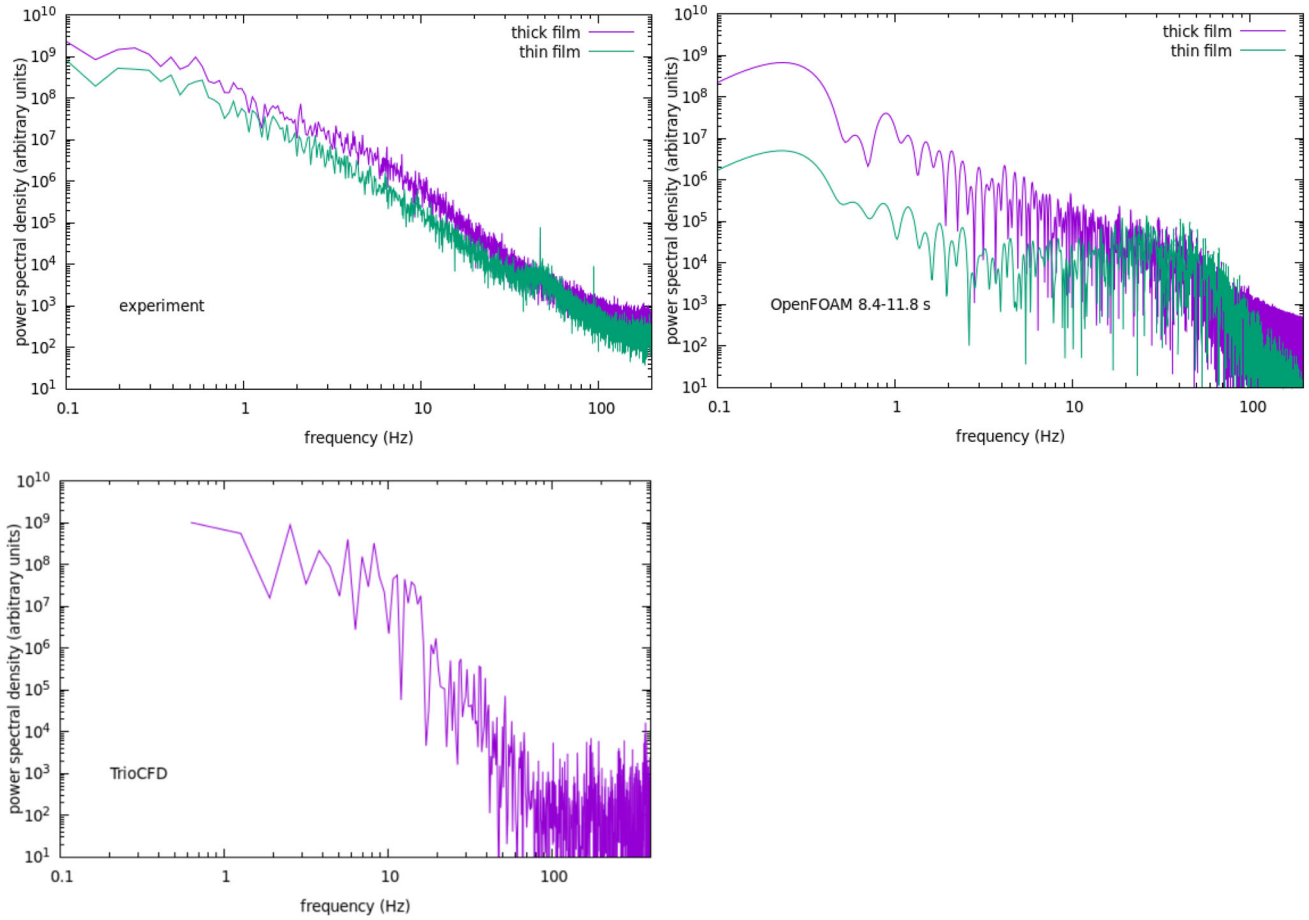

Fig. 14 Power spectra of interface disturbance waves at point 50 mm downstream the bubble's nose

two different computer codes and numerical schemes: OpenFOAM is using geometrical VOF interface tracking, while the TrioCFD code is based on explicit front tracking method. Considered Taylor bubble was observed in the inertia dominant regime, where the influence of viscosity and surface tension are minor.

The primary goal of this study was to compare the time-averaged shape of the Taylor bubble's interface. From the comparison between the experimental data and the OpenFOAM simulation—which used a model verified and validated on the case of a stagnant Taylor bubble in a laminar counter-current flow [22] —two main findings emerged:

- The bubble asymmetry in the simulation was more pronounced than that observed in the experiments, resulting in lower bubble drag and, consequently, a roughly 20% higher liquid mass flow rate needed to keep the bubble stationary.
- A less critical, but still relevant issue: fluctuations around the time-averaged bubble shape were weaker in the simulation than in the experiment.

The simulation of TrioCFD was performed with a more expensive numerical approach and only one second of transient was analyzed. This was not enough to develop an asymmetric bubble shape. Consequently, only qualitative bubble shape comparison was performed.

The second part of the study was focused on dynamics of interfacial waves traveling over the body of the Taylor bubble. Our analyses of various experiments in [37] have shown that the disturbance wave velocity, measured over a sufficiently long interval of several tens of seconds, becomes equal to the axial water–air interface velocity. The cross-correlation measurements primarily capture low-frequency waves, which are slower than the interface velocity. Therefore, tracking these waves provides a technique for measuring the time-averaged interface velocity.

The same analysis of disturbance waves on the interface was performed in both numerical simulations, where the accuracy of the analyses was severely limited with the spatial discretization of both simulations. Refined mesh in the near-wall region was barely sufficient to capture the disturbance waves and to reconstruct their propagation velocities in OpenFOAM. The specific numerical approach of TrioCFD

was even less appropriate for disturbance velocity measurements and allowed only rough approximation. When the interface fell out of the refined mesh in the near-wall region into the coarse meshing in the center of the pipe in OpenFOAM simulation, disturbance waves were not recognized anymore.

Spectra of the interfacial waves were compared at a point fixed from the bubble's nose. TrioCFD showed greater precision than OpenFOAM, accurately reflecting the sharp frequency decline above 10–20 Hz observed in experiments. In contrast, OpenFOAM's spectra erroneously displayed significant frequencies up to 70 Hz, likely misrepresenting the physical phenomena.

The stagnant Taylor bubble in turbulent low-Reynolds counter-current flow was identified as a challenging test case for two advanced interface tracking models in the TrioCFD and OpenFOAM codes, even though they were both well validated in laminar conditions [22, 41]. We demonstrated that fine spatial resolution is necessary not only in the near-wall region, where the liquid boundary layer forms, but also at the interface itself. Future simulations with both codes will aim to enhance the subgrid models for interface friction and surface tension.

Acknowledgements The authors gratefully acknowledge financial support provided by Slovenian Research Agency, grant P2-0026 and Slovenia-CEA grant NC-0026. The TrioCFD computations were made possible by the granted access to the HPC resources of IDRIS under the allocation 2023-R0131010339 made by GENCI.

Funding Funding was provided by Javna Agencija za Raziskovalno Dejavnost RS, NC-0026, Iztok Tiselj, P2-0026

References

1. Wallis G.B.: One-Dimensional Two-Phase Flow. McGraw Hill, (1969)
2. Morgado, A.O.; Miranda, J.M.; Araújo, J.D.P.; Campos, J.B.L.M.: Review on vertical gas-liquid slug flow. Int. J. Multiph. Flow **85**, 348–368 (2016)
3. Zhou, G.; Prosperetti, A.: Violent expansion of a rising Taylor bubble. Phys. Rev. Fluids **4**, 073903 (2019)
4. Holagh, S.G.; Ahmed, W.H.: Critical review of vertical gas-liquid slug flow: an insight to better understand flow hydrodynamics' effect on heat and mass transfer characteristics. Int. J. Heat Mass Transf. **225**, 125422 (2024)
5. Liberzon, D.; Shemer, L.; Barnea, D.: Upward-propagating capillary waves on the surface of short Taylor bubbles. Phys. Fluids **18**, 048103 (2006)
6. Dumitrescu, D.T.: Strömung an einer Luftblase im senkrechten Rohr. Z. angew. Math. Mech. **23**, 139 (1943)
7. Martin, C.S.: Vertically downward two-phase slug flow. ASME J. Fluids Eng. **98**(4), 715 (1976)
8. Lu, X.; Prosperetti, A.: Axial stability of Taylor bubbles. J. Fluid Mech. **568**, 173–192 (2006)
9. Figueroa-Espinoza, B.; Fabre, J.: Taylor bubble moving in a flowing liquid in vertical channel: transition from symmetric to asymmetric shape. J. Fluid Mech. **679**, 432–454 (2011). https://doi.org/10.1017/jfm.2011.159
10. Fabre, J.; Figueroa-Espinoza, B.: Taylor bubble rising in a vertical pipe against laminar or turbulent downward flow: symmetric to asymmetric shape transition. J. Fluid Mech. **755**, 485–502 (2014). https://doi.org/10.1017/jfm.2014.429
11. Fershtman, A.; Babin, V.; Barnea, D.; Shemer, L.: On shapes and motion of an elongated bubble in downward liquid pipe flow. Phys. Fluids **29**, 112103 (2017). https://doi.org/10.1063/1.4996444
12. Abubakar, H.; Matar, O.: Linear stability analysis of Taylor bubble motion in downward flowing liquids in vertical tubes. J. Fluid Mech. **941**, A2 (2022). https://doi.org/10.1017/jfm.2022.261
13. Delfos, R.; Wisse, C.J.; Oliemans, R.V.A.: Measurement of air-entrainment from a stationary Taylor bubble in a vertical tube. Int. J. Multiph. Flow **27**, 1769–1787 (2001)
14. Kockx, J.P.; Nieuwstadt, F.T.M.; Oliemans, R.V.A.; Delfos, R.: Gas entrainment by a liquid film falling around a stationary Taylor bubble in a vertical tube. Int. J. Multiph. Flow **31**, 1–24 (2005)
15. Mikuž B., Kamnikar, J., Prošek, J., Tiselj, I.: Experimental observation of Taylor bubble disintegration in turbulent flow. Proc. In: 28th Int. Conf. Nuclear Energy for New Europe 9, (2019).
16. Crowe, C.T.; Troutt, T.R.; Chung, J.N.: Numerical Models for Two-Phase Turbulent Flows. Annu. Rev. Fluid Mech. **28**, 11–43 (1996)
17. Trujillo, M.F.: Reexamining the one-fluid formulation for two-phase flows. Int. J. Multiph. Flow **141**, 103672 (2021)
18. The OpenFOAM Foundation, OpenFOAM | Free CFD Software, (2022).
19. Hirt, C.; Nichols, B.: Volume of fluid (VOF) method for the dynamics of free boundaries. J. Comput. Phys. **39**, 201–225 (1981)
20. Sint, A.M.; Deen, N.; Kuipers, J.: Numerical simulation of gas bubbles behaviour using a three-dimensional volume of fluid method. Chem. Eng. Sci. **60**, 2999–3011 (2005)
21. Tryggvason, G.; Scardovelli, R.; Zaleski, S.: Direct Numerical Simulations Of Gas-Liquid Multi-Phase Flows. Cambridge University Press, Cambridge, New York (2011)
22. Kren, J.; Frederix, E.M.A.; Tiselj, I.; Mikuž, B.: Numerical study of Taylor bubble breakup in countercurrent flow using large eddy simulation. Phys. Fluids **36**(2), 023311 (2024). https://doi.org/10.1063/5.0186236
23. Cifani, P.; Michalek, W.; Priems, G.; Kuerten, J.; Geld, C.; Geurts, B.: A comparison between the surface compression method and an interface reconstruction method for the VOF approach. Comput. Fluids **136**, 421–435 (2016)
24. Dai, D.; Tong, A.Y.: Analytical interface reconstruction algorithms in the PLIC-VOF method for 3D polyhedral unstructured meshes. Int. J. Numer. Meth. Fluids **91**, 213–227 (2019)
25. Klein, M.; Ketterl, S.; Hasslberger, J.: Large eddy simulation of multiphase flows using thevolume of fluid method: part 1—governing equations and a priori analysis. Exp. Comput. Multiph. Flow **1**, 130–144 (2019)

26. Vreman, A.W.: An eddy-viscosity subgrid-scale model for turbulent shear flow: algebraic theory and applications. Phys. Fluids **16**, 3670–3681 (2004)
27. Unverdi, S.O.: A front-tracking method for viscous, incompressible, multi fluid flows. J. Comput. Phys. **100**(1), 25–37 (1992)
28. Tryggvason, G.; Bunner, B.; Esmaeeli, A.; Juric, D.; Al-Rawahi, D.; Tauber, W.; Han, J.; Nas, S.; Jan, Y.: A front-tracking method for the computations of multiphase flow. J. Comput. Phys. **169**(2), 708–759 (2001)
29. Mathieu, B.: Physical, experimental and numerical study of fundamental mechanisms involved in two-phase flows, Ph.D. Thesis, Université Aix-Marseille 1, 2003
30. Osher, S.; Fedkiw, R.P.: Level Set Methods: An Overview and Some Recent Results. J. Comput. Phys. **169**, 463–502 (2001)
31. Araújo, J.; Miranda, J.; Pinto, A.; Campos, J.: Wide-ranging survey on the laminar flow of individual Taylor bubbles rising through stagnant Newtonian liquids. Int. J. Multiph. Flow **43**, 131–148 (2012)
32. Morgado, A.; Miranda, J.; Araújo, J.; Campos, J.: Review on vertical gas–liquid slug flow. Int. J. Multiph. Flow **85**, 348–368 (2016)
33. Cerqueira, R.F.; Paladino, E.E.; Evrard, F.; Denner, F.; Wachem, B.: Multiscale modeling and validation of the flow around Taylor bubbles surrounded with small dispersed bubbles using a coupled VOF-DBM approach. Int. J. Multiph. Flow **141**, 103673 (2021)
34. Gutiérrez, E.; Balcázar, N.; Bartrons, N.; Rigola, J.: Numerical study of Taylor bubbles rising in a stagnant liquid using a level-set/moving-mesh method. Chem. Eng. Sci. **164**, 158–177 (2017)
35. Angeli P.E., Puscas M.A., Fauchet G., Cartalade A.: FVCA8 Benchmark for the stokes and navier-stokes equations with the TrioCFD Code. finite volumes for complex applications VIII - methods and theoretical aspects, (2017)
36. Mikuž B., Frederix E.M.A., Komen E.M.J., Tiselj I.: Taylor bubble behaviour in turbulent flow regime. Proceedings of the conference Computational Fluid Dynamics for Nuclear Reactor Safety (CFD4NRS-8), 12 (2020)
37. Kren, J.; Zajec, B.; Tiselj, I.; El Shawish, S.; Perne, Ž; Tekavčič, M.; Mikuž, B.: Dynamics of Taylor bubble interface in vertical turbulent counter-current flow. Int. J. Multiphase Flow **165**, 104482 (2023)
38. Tekavčič, M.; Končar, B.; Kljenak, I.: The concept of liquid inlet model and its effect on the flooding wave frequency in vertical air-water churn flow. Chem. Eng. Sci. **175**, 231–242 (2018). https://doi.org/10.1016/j.ces.2017.09.050
39. Xue, Y.; Stewart, C.; Kelly, D.; Campbell, D.; Gormley, M.: Two-phase annular flow in vertical pipes: a critical review of current research techniques and progress. Water **14**, 3496 (2022). https://doi.org/10.3390/w14213496
40. Slavchov, R.I.; Peychev, B.; Ismail, A.S.: Characterization of capillary waves: a review and a new optical method. Phys. Fluids **33**(10), 101303 (2021)
41. Giamagas, G.; Zonta, F.; Roccon, A.; Soldati, A.: Propagation of capillary waves in two-layer oil–water turbulent flow. J. Fluid Mech. **960**, A5 (2023). https://doi.org/10.1017/jfm.2023.189
42. Nop, R., Hamrit, G., Burlot, A., Bois, G., Mikuž, B., Tiselj, I.: The 3D DNS of a Taylor bubble in counter-current flow with a turbulent wake using the Front-Tracking method in TrioCFD. In: 32nd International conference : nuclear energy for new europe, Portorož, Slovenia, September 11–14, (2023).
43. Pan, L.; He, H.; Ju, P.; Hibiki, T.; Ishii, M.: Experimental study and modeling of disturbance wave height of vertical annular flow. Int. J. Heat Mass Transf. **89**, 165–175 (2015)
44. Lin, R.; Wang, K.; Liu, L.; Zhang, Y.; Dong, S.: Study on the characteristics of interfacial waves in annular flow by image analysis. Chem. Eng. Sci. **212**, 115336 (2020)
45. Frederix, E.M.A.; Komen, E.M.J.; Tiselj, I.; Mikuž, B.: LES of turbulent co-current Taylor Bubble flow. Flow Turbulence Combust. **105**, 471–495 (2020)
46. Taha, T.; Cui, Z.F.: CFD modelling of slug flow in vertical tubes. Chem. Eng. Sci. **61**(2), 676–687 (2006). https://doi.org/10.1016/j.ces.2005.07.022
47. Press W.H., Teukolsky, S.A., Vetterling, W.T., Flannery B.P.: Numerical recipes 3rd edition: the art of scientific computing. Cambridge Press, (2007).
48. Grishchenko, D.: KROTOS image analysis for water-corium interactions (KIWI). OECD SERENA project report DEN/DTN/STRI/LMA/NT/2011/009/0, CEA, France, (2011).
49. Consortium, Open source. "Salome Meca". Version 9.*, http://www.salome-platform.org/ (2023). Accessed 2023
50. Bergant, R.; Tiselj, I.: Near-wall passive scalar transport at high Prandtl numbers. Phys. Fluids **19**, 065105 (2007)
51. Brackbill, J.; Kothe, D.; Zemach, C.: A continuum method for modeling surface tension. J. Comput. Phys. **2**, 335–354 (1992)